Emergent Materials
https://doi.org/10.1007/s42247-021-00298-z

ORIGINAL ARTICLE

Comprehensive microstructural and optical characterization of the thermal stability of aluminum-titanium oxynitride thin films after high temperature annealing in air

R. Escobar-Galindo[1] · I. Heras[2] · E. Guillén[3] · F. Munnik[4] · I. Azkona[5] · M. Krause[4]

Received: 1 June 2021 / Accepted: 21 August 2021

Abstract
The thermal stability of two $Al_yTi_{1-y}(O_xN_{1-x})$ layers prepared by cathodic vacuum arc deposition with different oxygen content was studied after high temperature annealing of the samples in air. These layers were designed to be part of solar-selective coating (SSC) stacks. Compositional and microstructural characterization of the thin films was performed before and after the thermal treatment by elastic recoil detection (ERD), transmission electron microscopy, and Raman spectroscopy. $Al_yTi_{1-y}N$ sample was stable after 2 h of annealing at 450 °C. Initial stages of the formation of a surface oxide layer after annealing at 650 °C were observed both by ERD and Raman analysis. Contrarily, no changes were found after 2 h annealing treatment either at 450 and 650 °C in the composition and microstructure of $Al_yTi_{1-y}(O_xN_{1-x})$ sample. In both samples, the formation of a surface anatase TiO_2 film was reported after 2 h annealing at 800 °C. These compositional and microstructural changes were correlated with the optical properties determined by spectroscopic ellipsometry. A transition from metallic to dielectric behavior with increasing annealing temperature was observed. These results complete the durability studies on the designed SSC based on $Al_yTi_{1-y}(O_xN_{1-x})$ materials, confirming that these stacks withstand breakdown at 600 °C in air.

1 Introduction

Thin films and coatings are currently being applied as emergent materials in a wide range of high temperature applications such as thermal barrier coatings for gas-turbine engines [1], thin films gas sensors [2], energy conversion materials [3], or solar selective coatings for solar thermal energy plant receivers [4, 5]. These materials have to withstand aggressive environments characterized by high temperature, large temperature gradients, cyclic stresses, or the presence of oxidizing and corroding atmosphere [6]. Hence, an accurate knowledge of the variation of optical properties, composition, and microstructure with temperature in the range of 400 to 1000 °C is required prior to their application. The most common failure mechanisms related with high temperature or extreme conditions are internal stresses after thermal expansion, temperature-induce oxide growth [7], changes in the microstructure, intra and interlayer phase transitions, diffusion of internal layers to the surface, electrochemical corrosion, evaporation of volatile components, or combination of various modes [8]. In order to ensure a proper multifunctional performance, multilayered coatings are commonly employed in high temperature applications. In this regard, solar selective multilayer coatings (SSC) with high absorptance (α) in the solar spectral range (0.3–2.5 µm) and low thermal emittance (ε) in the infrared region (2.5–30 µm) are required for improving the performance of concentrating solar power (CSP) receivers [9, 10]. SSC deposited by physical vapor deposition (PVD) techniques are commercially applied in parabolic trough systems, working at temperatures below 400 °C and under vacuum environments [5]. For central receivers of solar tower plants operating at higher concentration factors

✉ R. Escobar-Galindo
rescobar1@us.es

1 Departamento de Física Aplicada I, Escuela Politécnica Superior, Universidad de Sevilla, Virgen de África 7, 41011 Sevilla, Spain

2 Advanced Center for Aerospace Technologies (CATEC), C/Wilbur y Orville Wright 19, La Rinconada, 41309 Sevilla, Spain

3 Profactor GmbH, Im Stadtgut A2, 4407 Steyr-Gleink, Austria

4 Helmholtz-Zentrum Dresden-Rossendorf, Bautzner Landstraße 400, 01328 Dresden, Germany

5 Metal Estalki S.L, Polígono Ugaldeguren II, 48170 Zamudio, Spain

Published online: 23 September 2021

(C > 100) and temperatures (T > 565 °C), the substitution of non-selective absorber paints (i.e., Pyromark® [11, 12]) by solar selective multilayer coatings could overcome the current limitations of this CSP technology in relation to operation temperature, efficiency, and costs [10, 13, 14]. Multilayer SSC, based on transition metal nitrides/oxynitrides/oxides, have recently received much attention due to their tuneable optical properties such as reflection, absorption, refractive index, and their high-temperature thermal stability. Niranjan et al. have recently reported a multilayer SSC of W/WAlSiN/SiON/SiO_2 with a solar absorptance of 0.955 and low thermal emittance of 0.10 [15, 16]. The samples exhibited excellent thermal stability in air (500 °C for 100 h) and in vacuum (700 °C for 200 h) ascribed to the formation of fine nano-multilayers of W_2N and AlSiN in the WAlSiN layer structure. A large number of similar multilayer coatings have been reported in literature, namely TiAlN/TiAlON/Si_3N_4 [17], TiAlSiN/TiAlSiON/SiO_2 [18], TiAlCrN/TiAlN/AlSiN [19], TiAlN/CrAlON/Si_3N_4 [20], AlSiN/AlSiON/$AlSiO_y$ [21], AlCrSiN/AlCrSiON/AlCrO [22], WAlN/WAlON/Al_2O_3 [23], $CrAlSiN_x$/$CrAlSiO_yN_x$/$SiAlO_x$ [24], $Cr_{0.96}Al_{0.04}N_{0.89}$/$Cr_{0.62}Al_{0.38}$ N/$Cr_{0.53}Al_{0.47}N_{1.12}$/$Al_2O_3$ [25], and MgO/Zr/MgO [26].

In a former publication [27], we designed multilayer stacks based on $Al_yTi_{1-y}(O_xN_{1-x})$ oxynitride films with variable O/N content to be used as solar selective coating for high-temperature applications. The reported work assessed the need of a comprehensive understanding of the chemical bonding and thin film composition in order to properly adjust the final solar selectivity of the stack. The durability of selected multilayers was studied after (i) asymmetric tests of 12 h at 450, 650, and 800 °C and (ii) 900 h of heating–cooling thermal cycles between 300 and 600 °C in air [28]. The designed SSC fulfilled the performance criterion for high-temperature SCC after the long-term thermal cycling between 300 and 600 °C in air. However, a noticeable oxidation to crystalline rutile-type TiO_2 was identified by GIXRD and ERD profiles after asymmetric treatment at 800 °C, leading to degradation of the optical properties. In order to get acquainted with the observed failure mechanisms, individual $Al_yTi_{1-y}(O_xN_{1-x})$ thin films were exposed to short-term asymmetric tests of 2 h at 450, 650, and 800 °C in air in this study. Their microstructure, elemental composition, chemical bonding, and optical properties were analyzed before and after the annealing using transmission electron microscopy (TEM), elastic recoil detection (ERD), and Rutherford backscattering spectrometry (RBS), Raman spectroscopy, and spectroscopic ellipsometry (SE). This comprehensive analysis could improve the reliability of $Al_yTi_{1-y}(O_xN_{1-x})$ multilayer stacks as coatings for new generation of parabolic trough or solar tower receivers [10].

2 Experimental

2.1 Thin film growth

A set of $Al_yTi_{1-y}(O_xN_{1-x})$ thin films was deposited on mirror-polished Inconel HAYNES ® 626 substrates using a commercial direct current (DC) non-filtered cathodic vacuum arc PL70 Platit setup. The deposition parameters applied for the $Al_yTi_{1-y}(O_xN_{1-x})$ samples can be found elsewhere [27] and are summarized in Table 1.

As they were optimized previously for similar nitride films in this CVA chamber [29], the substrate temperature (450 °C), the arc current (125 A), and the substrate bias (− 75 V) were kept as constant parameters in order to obtain samples with low residual stress and good adhesion. A single rectangular $Al_{67}Ti_{33}$ cathode was employed for all the depositions. The flow rate of the reactive gases O_2 and N_2 was varied. In this work, two $Al_yTi_{1-y}(O_xN_{1-x})$ thin film samples were analyzed. They are named #1 and #5 according to the notation used in previous works (see Table 2) [27, 28]. Samples were grown using only reactive gases (N_2 and O_2) without Ar gas assistance. As described in [27], cross-sectional scanning electron microscopy images of the samples were used to obtain the thickness of the deposited samples (see Table 2). It is worth noting that sample #5 was deposited on top of ~ 0.5 µm AlTiN in order to improve the layer adhesion to the substrate. No delamination was observed in any of the deposited thin films.

2.2 Thin film compositional and microstructural characterization

ERD analysis was used to determine the depth-resolved elemental composition of the samples. The measurements were carried out using an incident 43 MeV Cl^{7+} ion beam of a 6-MV tandem accelerator. The angle between the sample normal and the incoming beam is 75° and the scattering

Table 1 Common deposition parameters employed for $Al_yTi_{1-y}(O_xN_{1-x})$ samples grown by CVA PL70 Platit setup

Parameter	Value
Base pressure (Pa)	2×10^{-4}
Working pressure (Pa)	1.5
Deposition temperature (ºC)	450
Cathode stoichiometry	$Al_{67}Ti_{33}$
Cathode size (mm^2)	331 × 174
Discharge current (A)	125
Bias voltage at deposition stage (V)	− 75
Rotation speed of the substrate (rpm)	10
Distance to the substrate (mm)	150

Table 2 Gas flow parameters applied for $Al_yTi_{1-y}(O_xN_{1-x})$ thin film deposition and measured thicknesses of the deposited layers

Sample #	Coating type	Flow rates (sccm)			$O_2/(O_2+N_2)$ gas flow ratio (%)	Thickness (μm)
		Ar	N_2	O_2		
1	$Al_yTi_{1-y}N$	0	70	0	0	1.65
5	$Al_yTi_{1-y}(O_xN_{1-x})$	0	46	12	21.0	1.25

angle is 31° relative to the beam direction. The analyzed area is about 1.5×1.5 mm^2. The recoils have been detected with a Bragg ionization chamber using a full energy detection circuit for the ion energies and a fast timing circuit to obtain a Z-dependent signal (Z, atomic number) to separate ion species. Hydrogen has been detected with a separate solid-state detector covered by an 18-μm Al foil to stop other scattered ions and recoils at a scattering angle of 41°. With this experimental configuration, the ERD spectra of all elements are obtained, and moreover the RBS spectrum of Ti (and possible heavy element impurities). All spectra were fitted simultaneously using the program NDF v9.3 g [30].

The microstructure was analyzed by cross-sectional transmission electron microscopy (TEM) with a TECNAI F30 microscope operated at 300 kV accelerating voltage. It is equipped with a Schottky-type field emission gun and an ultra-high resolution pole piece. The thin lamellas required for the cross-section analysis were made using a Focused Ion Beam (FIB) Dual Beam Helios 650 microscope. It is equipped with a 30-kV Ga focused ion beam source combined with a 30 kV electron beam placed at 52° between them, and with the Omniprobe® manipulator. Sample-protecting Pt thin films were deposited by electron beam deposition of $(CH_3)_3(C_pCH_3)Pt$.

Micro-Raman spectra were recorded on a LabramHR spectrometer (Horiba), situated at Helmholtz Zentrum Dresden-Rossendorf (HZDR). The system is equipped with a liquid N_2 cooled charge-coupled device detector and coupled to a BH2 microscope (Olympus). The laser beam of Nd:YAG solid-state laser with a wavelength of 532 nm was focussed to a spot diameter of 1 μm by a 50-fold magnifying objective. The laser power at the sample was 1 mW. The scattered light was collected in 180° backscattering geometry and dispersed by an 1800 line/mm grating. No sample degradation occurred under these conditions.

2.3 Determination of optical properties

The optical constants of the deposited thin films were determined by spectroscopic ellipsometry (SE) in the wavelength range of 211 to 1688 nm using a spectroscopic ellipsometer M-2000FI (J. A. Woollam, Inc.) with a fixed angle of polarized light incidence and reflection of 75°.

2.4 Single-stage thermal treatment test

Samples were subjected to short-term single-stage thermal treatment test that consists of a single heating cycle in an oven at atmospheric conditions, where the selected temperature (450, 650, or 800 °C) is kept constant for 2 h. These temperatures were selected as the current working temperature in parabolic trough plants is 450 °C while in tower plants, the current target temperature is 650 °C for molten salts and 800 °C for heat transfer fluids (currently) under development, respectively. A constant heating ramp of 5 °C/min was applied to reach the desired temperature. After 2 h, the sample was cooled down to room temperature inside the oven. The furnace employed for this test was a Nabertherm L9/11 with controller P330, equipped with SiC rod.

In Fig. 1, the appearance of #1 and #5 samples as-deposited at room temperature (RT) and after in air thermal exposition at 450 °C, 650, and 800 °C for 2 h is depicted.

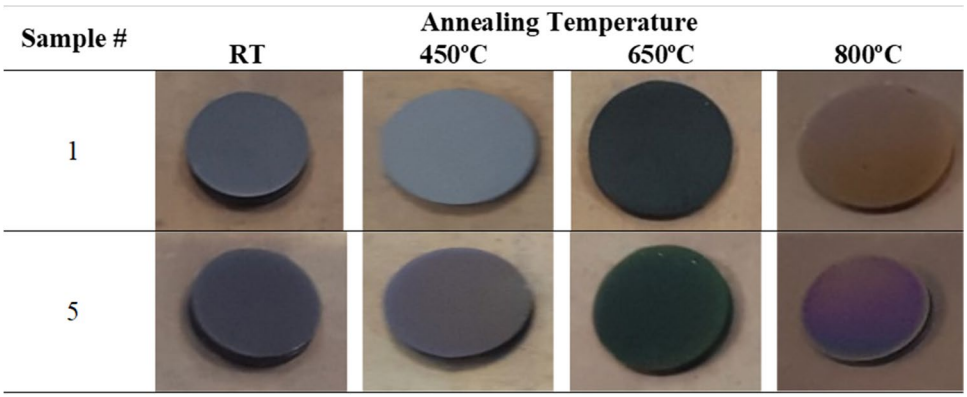

Fig. 1 Summary table showing #1 and #5 samples deposited on Inconel substrate at room temperature (RT) and after 2 h of thermal treatment in air at 450 °C, 650, and 800 °C

3 Results and discussion

The ERD elemental depth profiles of the $Al_yTi_{1-y}(O_xN_{1-x})$ samples #1 and #5 are displayed in Figs. 2 and 4, where the depth in at/cm^2 (areal density) are directly obtained from the measurements. This unit can be converted to nm using an estimated density of the layer obtained by taken the weighted mean of the atomic densities. The formula used for the conversion is as follows:

$$t = \frac{N_M \cdot < M_Z >}{\rho \cdot N_A} \quad (1)$$

with t the thickness in cm, N_M the areal density in at/cm^2, $< M_z > = \Sigma f_Z \cdot M_Z$ the average atomic mass in g/mol (with f_Z and M_Z the atomic fraction and the atomic weight of element Z, respectively), ρ the density in g/cm^3, and N_A Avogadro's number (mol^{-1}). The depth profiles are based on the recoil spectra except for Ti, for which also the profile based on the Cl^{+7} backscattering spectrum (marked as Ti (RBS)) is displayed in order to increase the information depth for this element. As explained in [27], the analysis depth limit is different for each element due to limitations in the separation of each recoil ion from the scattered Cl ions. This is reflected in the graphs by the abrupt drop of the ERD intensity for the elements Al and Ti. The elemental concentration of the as-deposited and after heated #1 and #5 samples measured by ERD analysis is summarized in Table 3. The elemental concentrations are based on a sample model that is fitted to the measured spectra. The concentrations

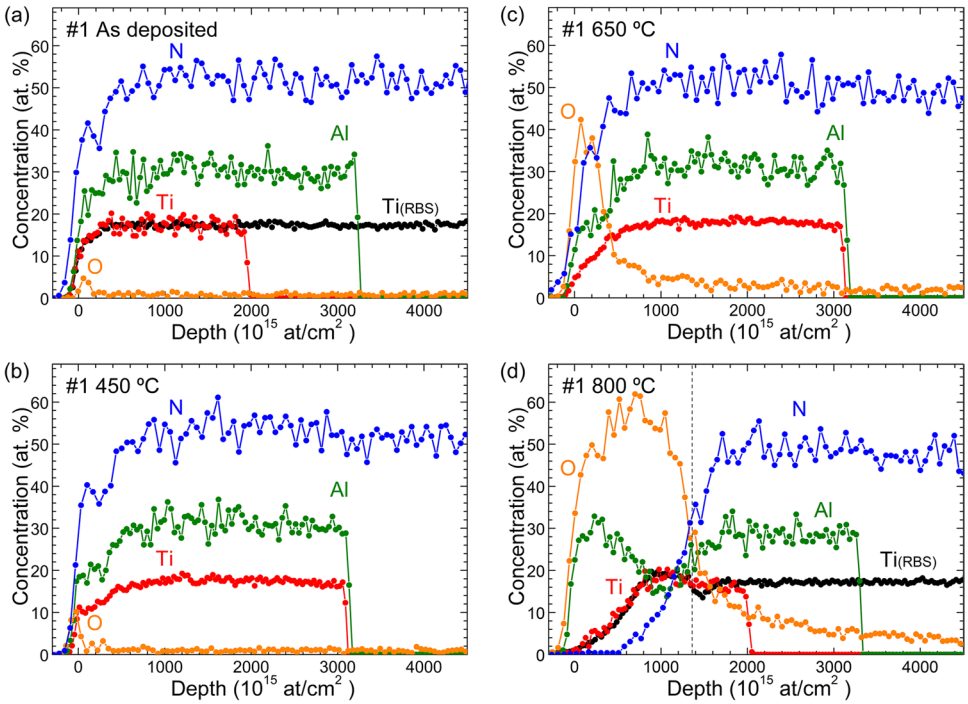

Fig. 2 ERD ion beam analysis of #1 AlTiN sample deposited on Inconel substrate at (**a**) RT, and after 2 h of thermal treatment in air at (**b**) 450ºC, (**c**) 650ºC and (**d**) 800ºC. In (**d**) a vertical dashed line indicates the approximated thickness of the oxide scale

Table 3 Elemental composition of as-deposited and after heated $Al_yTi_{1-y}(O_xN_{1-x})$ #1 and #5 samples. The estimated uncertainty is ± 0.5 at. %

#	Coating type	Temperature (°C)	Elemental composition (at.%)					
			O	N	Ti	Al	C	H
1	AlTiN	As-deposited	0.5	52.0	17.0	30.0	0.5	0.0
		450	1.0	51.0	17.0	30.5	0.5	0.0
		650	2.0	49.0	17.5	31.0	0.5	0.0
		800 (bulk layer)	6.5	48.0	17.0	28.0	0.5	0.0
		800 (top oxide)	58.0	3.5	15.0	23.0	0.5	0.0
5	$Al_yTi_{1-y}(O_xN_{1-x})$	As-deposited	20.0	35.0	15.0	30.0	0.5	0.5
		450	20.5	34.0	15.5	29.5	0.5	0.0
		650	21.0	33.5	15.5	29.5	0.5	0.0
		800 (bulk layer)	20.0	34.5	15.0	30.0	0.5	0.0
		800 (top oxide)	59.5	3.0	11.0	26.0	0.5	0.0

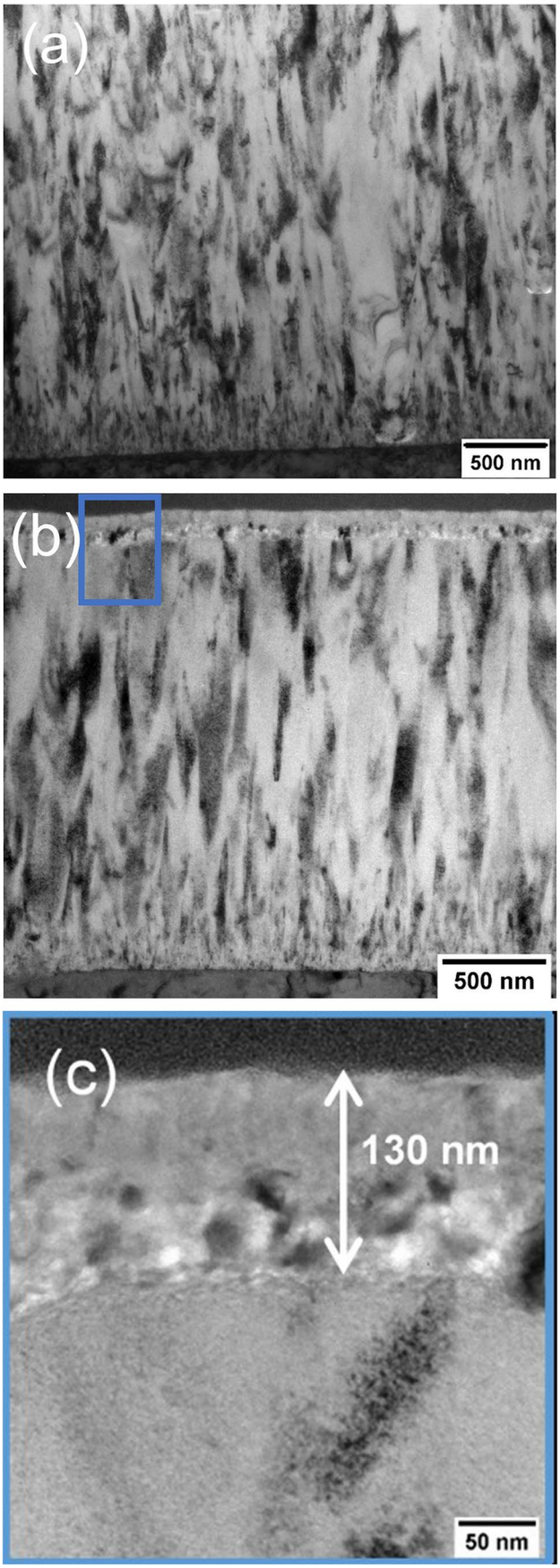

Fig. 3 HR-TEM images of #1 AlTiN sample deposited on Inconel ▶ substrate at (**a**) RT, and after 2 h of thermal treatment in air at (**b**) 800 °**C**. In **c**, an amplified HR-TEM image of the ~ 130 nm oxidized region marked in **b** with a blue rectangle is shown

were calculated from the main part of the layer, excluding the surface region with elevated oxygen concentrations, where the effects of roughness or interface mixing are also visible.

Figure 2 shows the ERD ion beam analysis results of the as-deposited and after heated at 450, 650, and 800 °C sample #1. ERD analysis on the as-deposited sample #1 reveals a homogeneous AlTiN layer along the thickness of the sample before the film was subjected to high temperature (Fig. 2(a)). This is confirmed by the HR-TEM cross-section image of the as-deposited sample shown in Fig. 3.

As reported in [27], the film exhibits a clear columnar growth only interrupted by defects attributed to the release of macroparticles during the deposition process [31]. In that work, selective area electron diffraction (SAED) pattern revealed a polycrystalline structure of AlTiN corresponding to lattice plane distances of 2.4, 2.1, 1.5, 1.3, 1.2, and 0.9 Å, in good agreement with (111), (200), (220), (311), (222), and (400) reference values of *fcc*-Al0.5Ti0.5 N (ICCD card 04–018-6856). No changes in the composition were found after the 2-h annealing treatment at 450 °C (Fig. 2(b)) in accordance with the thermal stability reported earlier for solar-selective coatings based on aluminum titanium nitrides at such temperatures [28, 32]. In Fig. 2(c), the initial stages of the formation of an aluminum-titanium oxide layer on top of the AlTiN #1 sample after annealing at 650 °C were observed. This is in good agreement with a previous study reported in literature where a combined analysis of RBS and X-ray absorption spectroscopy (XAS) showed the formation of a protective Al-Ti–O layer as a result of a 2-h annealing of AlTiN at 700 °C in an $Ar + O_2$ atmosphere [33]. Finally, after 800 °C annealing, a surface Al_2O_3 layer is fully formed followed by a mixed Al-Ti oxide layer (see dashed line in Fig. 2(d)). The original AlTiN layer composition is well preserved underneath these oxides although some interdiffusion of oxygen could be detected. Assuming a density $\rho = 3.95$ g/cm^3 (typical value for Al_2O_3), the formation of an oxide scale of ~ 120 nm after annealing at 800 °C could be derived from Eq. (1). HR-TEM images in Fig. 3b and c confirmed the formation of these oxide films, estimating a total thickness of the scale of ~ 130 nm in very good agreement with the thickness calculated by ERD.

Figure 4 shows the ERD ion beam analysis results of the as-deposited and after heated at 450, 650, and 800 °C sample #5. The as-deposited ERD spectrum of AlTiON #5 (Fig. 4(a)) exhibits a first region with a higher amount of oxygen, followed by a subsequent region with a constant 20% at. of oxygen. This first region was attributed

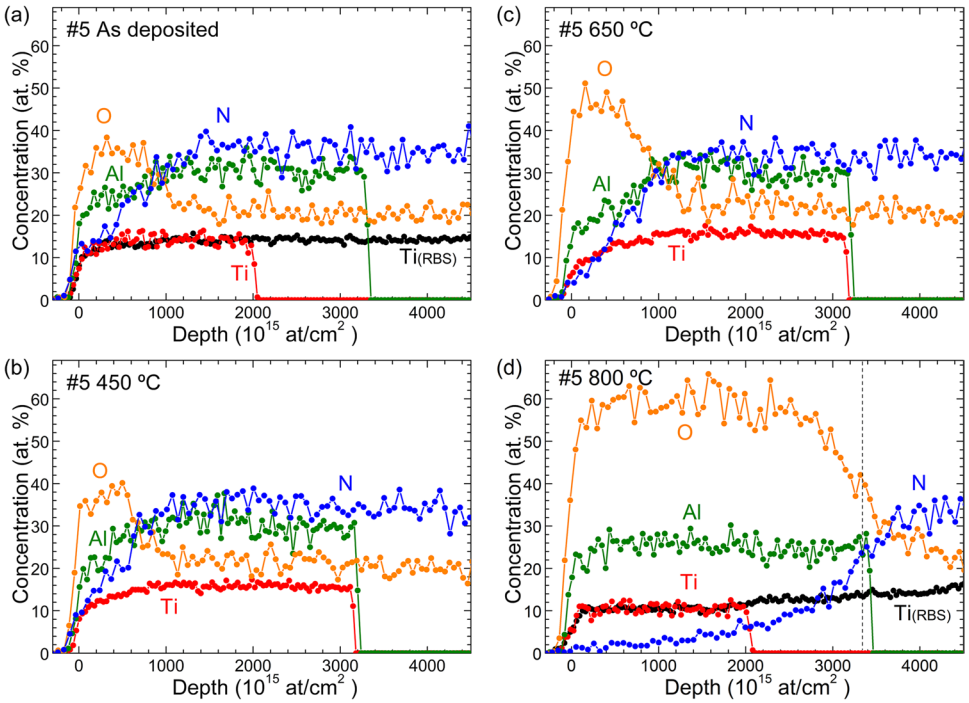

Fig. 4 ERD ion beam analysis of #5 AlTiON sample deposited on Inconel substrate at (**a**) RT, and after 2 h of thermal treatment in air at (**b**) 450 °C, (**c**) 650 °C, and (**d**) 800 °C. In d, a vertical dashed line indicates the approximated thickness of the oxide scale

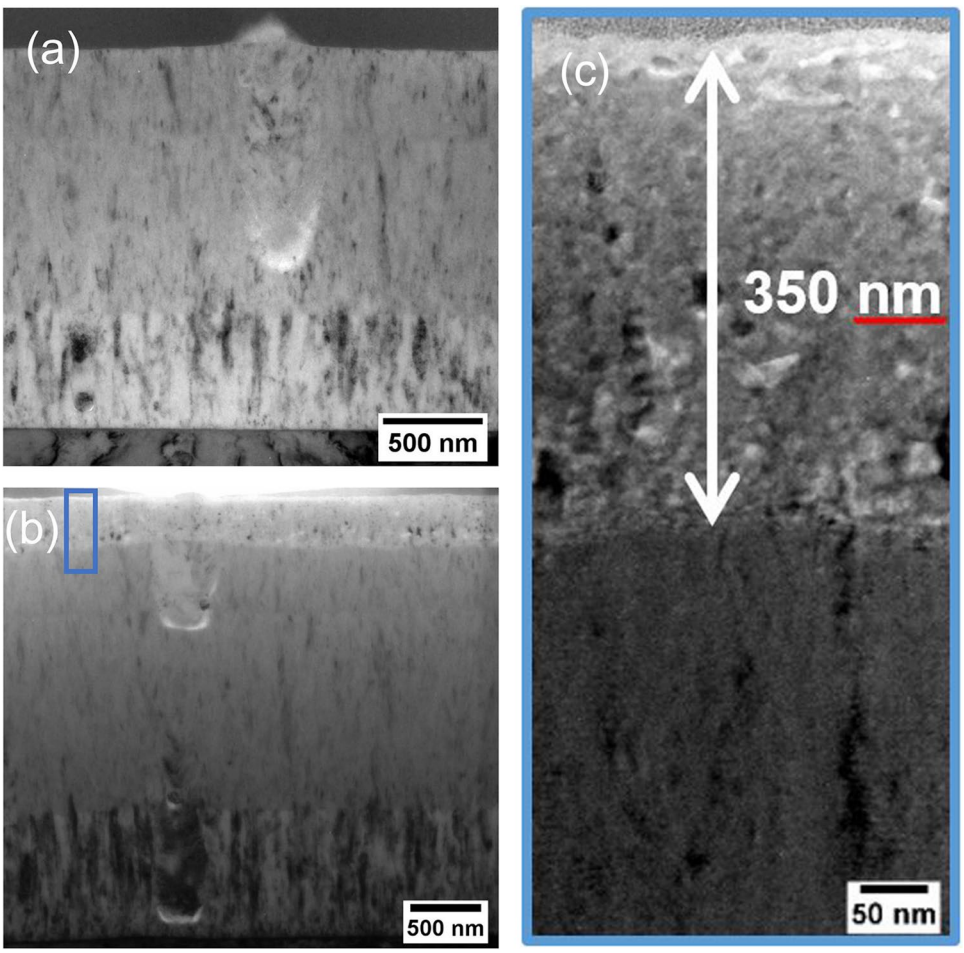

Fig. 5 HR-TEM images of #5 AlTiON sample deposited on Inconel substrate at (**a**) RT, and after 2 h of thermal treatment in air at (**b**) 800 °C. In **c**, an amplified HR-TEM image of the ~ 350 nm oxidized region marked in **b** with a blue rectangle is shown

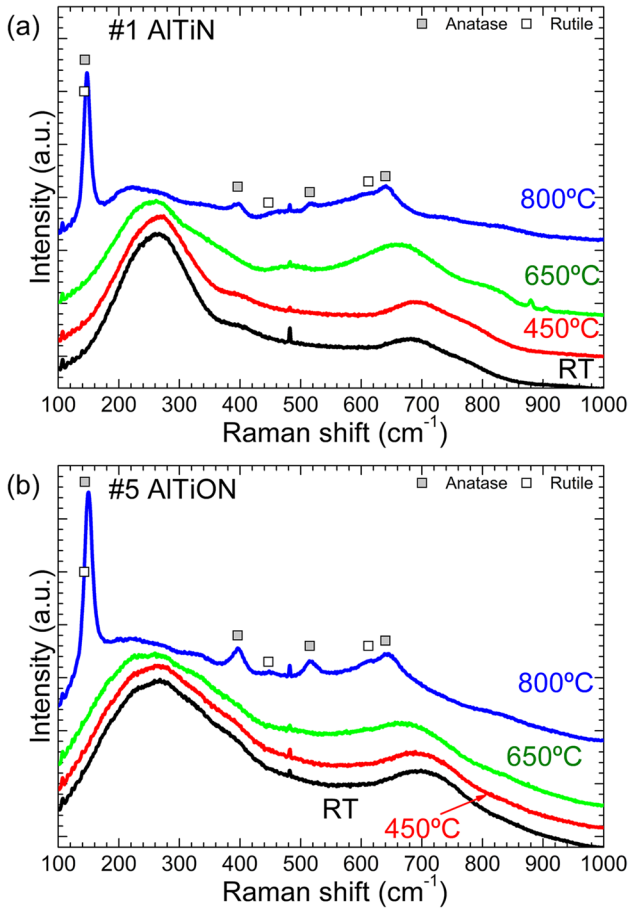

Fig. 6 Raman spectroscopy analysis of (**a**) #1 AlTiN and (**b**) #5 AlTiON samples deposited on Inconel substrate at RT and after 2 h of thermal treatment in air at 450 °C, 650 °C, and 800 °C. The weak and sharp peak at ~ 480 cm^{-1} is due to the Hg-e line emission from outward of the Raman lab

in [27] to surface roughness which causes that the spectra are more rounded in the surface region compared to the simulation without surface roughness [34]. Moreover, the HR-TEM cross-section image of the as-deposited sample #5 (Fig. 5(a)) showed no evidence of the creation of an oxide layer on top of the AlTION #5. The abrupt change of morphology and image contrast at a thickness of 500 nm corresponds to the interface between AlTiON #5 and AlTiN #1 interlayer. The interplanar distances calculated from SAED in the #5 sample were 2.5, 2.1, 1.5, and 1.2 and correspond to (111), (200), (220), and (222) planes of *fcc*-Al0.5T0.5 N (ICCD card 04–018-6856), respectively, without any evidence of crystalline Al_2O_3 or TiO_2 formation [27]. No significant changes in the composition of #5 sample were found after the 2-h annealing treatment either at 450 (Fig. 4(b)) or 650 °C (Fig. 4(c)). These results confirmed the higher thermal stability of aluminum titanium oxynitrides (21 at.% O) as compared to the pure AlTiN film of sample #1 (0 at.% O). In fact, in [28], it was reported a better optical performance for solar-selective multilayer coatings containing aluminum titanium oxynitrides. Finally, after 800 °C annealing, the ERD spectrum of #5 showed 3 different zones (see Fig. 4(d)): (1) a homogeneous mixed oxide on top, probably $(Al,Ti)_2O_3$, with an estimated thickness of ~ 290 nm according to Eq. (1) is followed by (2) a transition interlayer where oxygen and nitrogen content are gradually changing until reaching (3) the pristine AlTiON #5 layer. HR-TEM images in Fig. 5(b and c) confirmed the formation of these oxide films, estimating the total thickness of the oxide scale to be of ~ 350 nm again in very good agreement with the thickness calculated by ERD.

The compositional and microstructural characterization was completed by performing Raman spectroscopy on the as-deposited and annealed #1 and #5 samples. Raman spectra of the as-deposited AlTiN #1 and AlTiON #5 films show two broad bands centered at ≈ 265 and ≈ 690 cm^{-1}, as can be seen in Fig. 6(a and b), respectively. As demonstrated in previous publication [27], these samples have *fcc*-cubic crystalline structure, which means that every ion is at a site of inversion symmetry and that there are no first-order allowed Raman active phonon vibration. Consequently, the observed bands represent the phonon-density of states (P-DOS) of the samples. In first approximation, the lower energetic bands can be attributed to the P-DOS of the heavier elements Ti and Al, the higher energetic one to that of N and/or O. The P-DOS-type Raman spectrum of both samples did not change at all during in-air treatment at 450 °C. After heating to 650 °C, the two broad band Raman characteristics is conserved, but a slight downshift of the higher-energetic Raman band to ≈ 660 cm^{-1} occurred. This downshift reflects the increased concentration of oxygen in both samples. A qualitative change of the Raman spectra is found after heating at 800 °C. For both samples, distinct Raman lines at ≈ 148 cm^{-1}, ≈ 396 cm^{-1}, ≈ 516 cm^{-1}, and ≈ 641 cm^{-1} demonstrate the formation of crystalline Anatase-type TiO_2 [35, 36]. The most intense anatase mode, E_g observed at 148 cm^{-1}, is slightly blue shifted as compared to pure anatase TiO_2 (144 cm^{-1}). A blue shift of this line has been reported for Anatase-type TiO_2 nanoparticles and ascribed to phonon confinement and oxygen sub-stoichiometry [37, 38]. Moreover, the Raman spectra of both samples indicate two more new features at ≈ 450 cm^{-1} and at ≈ 610 cm^{-1} that hint to fractions of Rutile-type TiO_2 [39]. The much higher relative intensity of the Anatase-type compared to the Rutile-type Raman lines cannot be attributed to a resonant Raman effect, since the band gap of both polymorphs are similar, with 3.2 eV for Anatase and 3.0 eV for Rutile, respectively [40]. Thus, this observation points to the preferred formation of Anatase-type TiO_2 in the studied samples. This is surprising since the Rutile modification is thermodynamically more stable at 800 °C, and it was the only TiO_2 phase

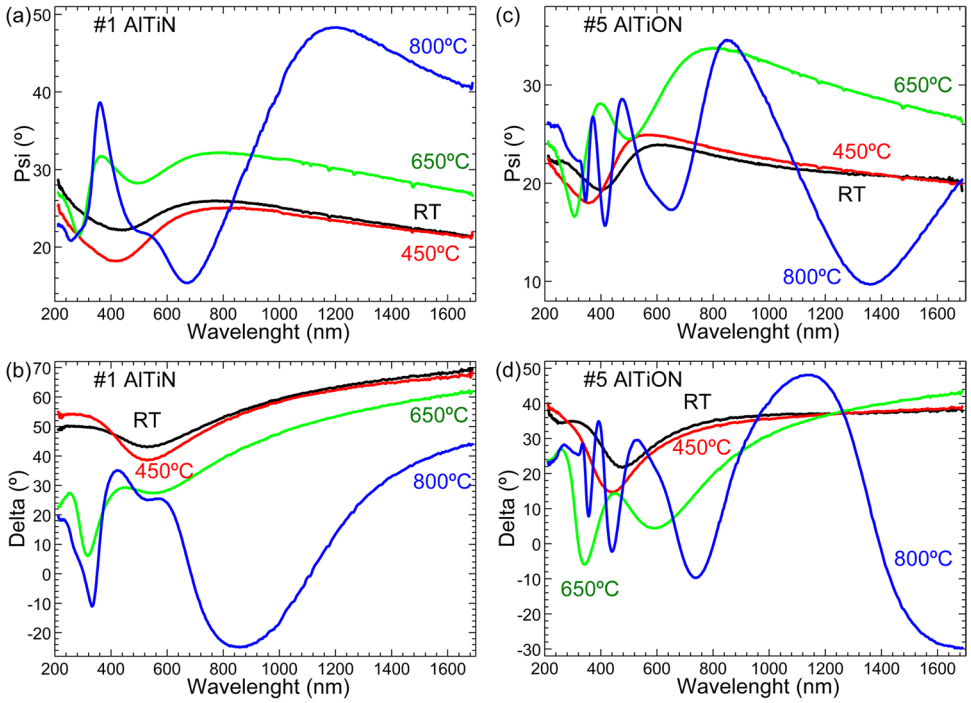

Fig. 7 Ellipsometry parameters (ψ, Δ) of #1 (**a**, **b**) and #5 (**c**, **d**) deposited samples on Inconel substrate at RT and after 2 h of thermal treatment in air at 450 °C, 650 °C, and 800 °C

observed after in-air heating of complete $Al_yTi_{1-y}(O_xN_{1-x})$ SSC at 800 °C [28]. On the other hand, Anatase is preferentially formed at lower temperatures during thin film growth [41]. Thus, it might be argued that the precursors AlTiN and AlTiON lead preferentially to Anatase-type TiO_2, while, if the oxidation starts from a TiN interlayer [27], the Rutile-type modification is dominant.

The abovementioned compositional and microstructural changes observed by ERD, HR-TEM, and Raman after the short-term single-stage thermal treatment tests up to 800 °C had a direct correlation with the optical response (as measured by spectroscopic ellipsometry) of the studied samples. In Fig. 7, the ellipsometric parameters ψ and Δ of #1 and #5 samples deposited on Inconel substrate at room temperature and after 2 h of thermal treatment in air at 450 °C, 650 °C, and 800 °C are shown. As described in [27], the as-deposited #1 and #5 samples could be fitted using one Lorentz and two Gauss oscillators in the range from 211 to 1688 nm. The absorbing character of the layers is well preserved after the short-term treatment at 450 °C as both ellipsometric parameters showed no noticeable changes. However, after 650 °C, the higher sensitivity of the SE revealed a change in the optical behavior of the annealed samples. In particular, the psi spectra of Fig. 7 evolved towards a characteristic shape with pronounced oscillations typical of transparent materials in the VIS range. This observation is consistent with the formation of a thin top oxide on both samples after 650 °C as detected by ERD, being this oxide thicker for the #5 sample. Finally, after annealing at 800 °C, both samples developed a thick Al-Ti oxide layer. This is clearly reflected in the drastic change in the ellipsometry parameters observed in Fig. 7 and it is correlated with the formation of oxide scales of ~ 130 nm and ~ 350 nm, for samples #1 and #5, respectively, as measured both by ERD and TEM. Moreover, in the optical images of Fig. 1, a clear change in the color of the samples after 800 °C is observed.

4 Conclusions

Two $Al_yTi_{1-y}(O_xN_{1-x})$ layers prepared by cathodic vacuum arc deposition with different oxygen content (#1 [O] = 0 at.%, #5 [O] = 21 at.%) were evaluated after 2 h of annealing in air at 450, 650, and 800 °C. Both samples showed no compositional (ERD), structural (Raman), or optical (SE) modification after the annealing treatment at 450 °C. ERD and Raman revealed the initial formation of an aluminum-titanium oxide layer on top of the AlTiN #1 layer after the annealing treatment at 650 °C. Sample AlTION #5 presented a higher thermal stability at this temperature with no significant compositional changes. However, the slight increase of the oxygen concentration found by ERD and the slight downshift detected for the higher-energetic Raman band to ≈ 660 cm^{-1} are ascribed to an increased oxygen concentration also in this sample. These observations are good agreement with the gradual transition from metallic to dielectric optical behavior observed by SE at this annealing temperature. A complete oxidation of both films was reported after 2 h annealing at 800 °C. Raman observation conclude to the preferred formation of Anatase-type TiO_2 in

the studied annealed samples at 800 °C, although the presence of Rutile-type TiO_2 cannot be discarded. In a previous work [27], Rutile-type TiO_2 was the only oxide present after in-air heating at 800 °C of complete SSC stacks using $Al_yTi_{1-y}(O_xN_{1-x})$ layers and a TiN interlayer. Hence, it can be claimed that the individual $Al_yTi_{1-y}(O_xN_{1-x})$ layers promote the formation of Anatase while in the complete stack, the oxidation of the TiN interlayer leads to a Rutile-type formation. These results complete the durability studies on the designed SSC based on $Al_yTi_{1-y}(O_xN_{1-x})$ materials, confirming that these stacks withstand breakdown at 600 °C in air. However, the formation of Al-Ti–O layers at 800 °C hinder the application of these stacks at higher temperatures. In this regard, the substitution of titanium for chromium and the application of $Al_yCr_{1-y}(O_xN_{1-x})$ layer with a higher oxidation resistance could be considered [25].

Acknowledgements Support by the Ion Beam Centre (IBC, Helmholtz-Zentrum Dresden-Rossendorf) is gratefully acknowledged. The authors would like to thank R. Heller F. Lungwitz and A. Schneider (Helmholtz-Zentrum Dresden – Rossendorf) for assistance during the use of IBA, thermal treatments, and Raman spectrometer at the IBC and A. Mayoral (Laboratorio de Microscopias Avanzadas from Instituto de Nanociencia de Aragón) for offering access to their instruments and expertise with TEM measurement.

Funding This project was partially supported by H2020 RISE project "*Framework of Innovation for Engineering of New Durable Solar Surfaces* (FRIENDS2, GA-645725)," by the Spanish Ministry of Science and Innovation project "*Recubrimientos innovadores preparados por magnetron sputtering para absorción solar selectiva* (MAGICOS2, PID2019-104256RB-I00)," and by the Agencia Estatal de Investigacion (AEI) project "*Entrenamiento avanzado en materiales para superficies solares duraderas* (EIN2020-112163/AEI/10.13039/501100011033)."

Declarations

Conflict of interest The authors declare no competing interests.

References

1. D.R. Clarke, M. Oechsner, N.P. Padture, Thermal-barrier coatings for more efficient gas-turbine engines. MRS Bull. **37**(10), 891–898 (2012). https://doi.org/10.1557/mrs.2012.232
2. Z.M. Seeley, A. Bandyopadhyay, S. Bose, Titanium dioxide thin films for high temperature gas sensors. Thin Solid Films **519**(1), 434–438 (2010). https://doi.org/10.1016/j.tsf.2010.07.040
3. P.E. Gannon, C.T. Tripp, A.K. Knospe, C.V. Ramana, M. Deiberta, R.J. Smith, V.I. Gorokhovsky, V. Shutthanandan, D. Gelles, High-temperature oxidation resistance and surface electrical conductivity of stainless steels with filtered arc Cr–Al–N multilayer and/or superlattice coatings. Surf. Coat. Technol. **188–189**, 55–61 (2004). https://doi.org/10.3390/met11030405
4. C.K. Ho, B.D. Iverson, Review of high-temperature central receiver designs for concentrating solar power. Renew. Sustain. Energy Rev. **29**, 835–846 (2014). https://doi.org/10.1016/j.rser.2013.08.099
5. N. Selvakumar, H.C. Barshilia, Review of physical vapor deposited (PVD) spectrally selective coatings for mid- and high-temperature solar thermal applications. Sol. Energy Mater. Sol. Cells **98**, 1–23 (2012). https://doi.org/10.1016/j.solmat.2011.10.028
6. S. Bose, High temperature coatings, 2nd ed.; Butterworth-Heineman, (2018), https://doi.org/10.1016/C2015-0-01316-8.
7. A.G. Evans, D.R. Mumm, J.W. Hutchinson, Prog. Mater. Sci. **46**, 505–553 (2001). https://doi.org/10.1016/S0079-6425(00)00020-7
8. B. Carlsson, K. Möller, M. Köhl, M. Heck, S. Brunold, U. Frei, J.C. Marechal, G. Jorgensen, The applicability of accelerated life testing for assessment of service life of solar thermal components, Sol. Energy Mater. Sol Cells **84**, 255–274 (2004). https://doi.org/10.1016/j.solmat.2004.01.046
9. Q.-C. Zhang, Recent progress in high-temperature solar selective coatings. Sol. Energy Mater. Sol. Cells **62**, 63–74 (2000). https://doi.org/10.1016/S0927-0248(99)00136-1
10. R. Escobar-Galindo, M. Krause, K. Niranjan, H.C. Barshilia, Solar selective coatings and materials for high-temperature solar thermal applications in Sustainable Material Solutions for Solar Energy Technologies (Elsevier, 2021).
11. S. Wijewardane, D.Y. Goswami, A review on surface control of thermal radiation by paints and coatings for new energy applications. Renew. Sustain. Energy Rev. **16**, 1863–1873 (2012). https://doi.org/10.1016/j.rser.2012.01.046
12. C.K. Ho, A.R. Mahoney, A. Ambrosini, M. Bencomo, A. Hall, T.N. Lambert, Characterization of Pyromark 2500 for high-temperature solar receivers. ASME. J. Sol. Energy Eng. **136**(1), 014502 (2014). https://doi.org/10.1115/1.4024031
13. H.L. Zhang, J. Baeyens, J. Degrève, G. Cacères, Concentrated solar power plants: Review and design methodology. Renew. Sustain. Energy Rev. **22**, 466–481 (2013)
14. F. Cao, K. McEnaney, G. Chen, Z. Ren, Review of cermet-based spectrally-selective solar absorbers. Environ. Sci. **7**, 1615–1627 (2014). https://doi.org/10.1039/C3EE43825B
15. K. Niranjan, P. Kondaiah, G. Srinivas, H.C. Barshilia, Optimization of W/WAlSiN/SiON/SiO2 tandem absorber consisting of double layer anti-reflection coating with broadband absorption in the solar spectrum region. Appl. Surf. Sci. **496**, 143651 (2019). https://doi.org/10.1016/j.apsusc.2019.143651
16. K. Niranjan, A. Soum-Glaude, A. Carling-Plaza, S. Bysakh, S. John, H.C. Barshilia, Extremely high temperature stable nanometric scale multilayer spectrally selective absorber coating: Emissivity measurements at elevated temperatures and a comprehensive study on ageing mechanism. Sol. Energy Mater. Sol. Cells **221**, 110905 (2021). https://doi.org/10.1016/j.solmat.2020.110905
17. H.C. Barshilia, N. Selvakumar, K.S. Rajam, D.V. Sridhara Rao, K. Muraleedharan, A. Biswas, TiAlN/TiAlON/Si_3N_4 tandem absorber for high-temperature solar selective applications. Appl. Phys. Lett. **89**, 191909 (2006). https://doi.org/10.1063/1.2387897
18. L. Rebouta, P. Capela, M. Andritschky, A. Matilainen, P. Santilli, K. Pischow, E. Alves, Characterization of TiAlSiN/TiAlSiON/

SiO_2 optical stack designed by modelling calculations for solar selective applications. Sol. Energy Mater. Sol. Cells **105**, 202–207 (2012). https://doi.org/10.1016/j.solmat.2012.06.011
19. K. Valleti, D. Murali Krishna, S.V. Joshi, Functional multilayer nitride coatings for high temperature solar selective applications. Sol. Energy Mater. Sol. Cells **121**(14), 21 (2014). https://doi.org/10.1016/j.solmat.2013.10.024
20. N. Selvakumar, H.C. Barshilia, Review of physical vapor deposited (PVD) spectrally selective coatings for mid- and high- temperature solar thermal applications. Sol. Energ. Mat. Sol. Cells **98**, 1–23 (2012). https://doi.org/10.1016/j.solmat.2011.10.028
21. L. Rebouta, A. Sousa, M. Andritschky, F. Cerqueira, C.J. Tavares, P. Santilli, K. Pischow, Solar selective absorbing coatings based on AlSiN/AlSiON/$AlSiO_y$ layers. Appl. Surf. Sci. **356**, 203–212 (2015). https://doi.org/10.1016/j.apsusc.2015.07.193
22. C. Zou, W. Xie, L. Shao, Functional multi-layer solar spectral selective absorbing coatings of AlCrSiN/AlCrSiON/AlCrO for high-temperature applications. Sol. Energy Mater. Sol. Cells **153**, 9–17 (2016). https://doi.org/10.1016/j.solmat.2016.04.007
23. A. Dan, J. Jyothi, K. Chattopadhyay, H.C. Barshilia, B. Basu, Spectrally selective absorber coating of WAlN/WAlON/Al_2O_3 for solar thermal applications. Sol. Energy Mater. Sol. Cells **157**, 716–726 (2016). https://doi.org/10.1016/j.solmat.2016.07.018
24. A. Al-Rjoub, P. Costa, L. Rebouta, I.B. Radović, K. Arstila, N.P. Barradas, E. Alves, A. Matilainen, K. Pischow, A study of solar thermal absorber stack based on CrAlSiNx/CrAlSiNxOy structure by ion beams Nucl. Instruments Methods Phys. Res. Sect. B Beam Interaction with Mater. Atoms **450**, 195–199 (2019). https://doi.org/10.1016/j.nimb.2018.04.024
25. T.C. Rojas, A. Caro, R. Escobar-Galindo, J.C. Sánchez-López, High temperature solar selective coatings based on Cr(Al)N Part 2: Design, spectral properties and thermal stability of multilayer stacks. Sol. Energy Mater. Sol. Cells **218**, 110812 (2020). https://doi.org/10.1016/j.solmat.2020.110812
26. Z.Y. Nuru, M. Msimanga, T.F.G. Muller, C.J. Arendse, C. Mtshali, M. Maaza, Microstructural, optical properties and thermal stability of MgO/Zr/MgO multilayered selective solar absorber coatings. Sol. Energy **111**, 357–363 (2015). https://doi.org/10.1016/j.solener.2014.11.009
27. I. Heras, E. Guillén, F. Lungwitz, G. Rincón-Llorente, F. Munnik, E. Schumann, I. Azkona, M. Krause, R. Escobar-Galindo, Design of high-temperature solar-selective coatings based on aluminium titanium oxynitrides $Al_yTi_{1-y}(O_xN_{1-x})$. Part 1: Advanced microstructural characterization and optical simulation. Sol. Energy Mater. Sol. Cells **176**, 81–92 (2018). https://doi.org/10.1016/j.solmat.2017.10.015
28. R. Escobar-Galindo, E. Guillén, I. Heras, G. Rincón-Llorente, M. Alcón-Camas, F. Lungwitz, F. Munnik, E. Schumann, I. Azkona, M. Krause, Design of high-temperature solar-selective coatings based on aluminium titanium oxynitrides $Al_yTi_{1-y}(O_xN_{1-x})$. Part 2: Experimental validation and durability tests at high temperature. Sol. Energy Mater. Sol. Cells **185**, 183–191 (2018). https://doi.org/10.1016/j.solmat.2018.04.027
29. J.M. Andersson, J. Vetter, J. Müller, J. Sjölén, Structural effects of energy input during growth of $Ti_{1-x}Al_xN$ ($0.55 \leq x \leq 0.66$) coatings by cathodic arc evaporation. Surf. Coat. Technol. **240**, 211–220 (2014). https://doi.org/10.1016/j.surfcoat.2013.12.018
30. N.P. Barradas, C. Jeynes, R.P. Webb, Simulated annealing analysis of Rutherford backscattering data. Appl. Phys. Lett. **71**, 291 (1997). https://doi.org/10.1063/1.119524
31. C. Ducros, C. Cayron, F. Sanchette, Multilayered and nanolayered hard nitride thin films deposited by cathodic arc evaporation. Part 1: deposition, morphology and microstructure. Surf. Coat. Technol. **201**, 136–142 (2006). https://doi.org/10.1016/j.surfcoat.2005.11.102
32. A. Schüler, P. Reimann, P. Oelhafen, G. Francz, T. Zehnder, M. Duggelin, D. Mathys, R. Guggenheim, Structural and optical properties of titanium aluminum nitride films ($Ti_{1-x}Al_xN$). J. Vac. Sci. Technol. A. **19**, 922 (2001). https://doi.org/10.1116/1.1359532
33. J.L. Endrino, G.S. Fox-Rabinovich, R. Escobar Galindo, W. Kalss, S. Veldhuis, L. Soriano, J. Andersson, A. Gutiérrez, Oxidation post treatment of hard AlTiN coating for machining of hardened steels. Surf. Coat. Technol. **204**(3), 256–262 (2009). https://doi.org/10.1016/j.surfcoat.2009.07.010
34. R. Behrisch, S. Grigull, U. Kreissig, R. Grötzschel, Influence of surface roughness on measuring depth profiles and the total amount of implanted ions by RBS and ERDA, Nucl. Instrum. Methods Phys. Res. Sect. B Beam Interact. Mater. At. **136–138**, 628–632 (1998). https://doi.org/10.1016/S0168-583X(97)00798-2
35. T. Ohsaka, F. Izumi, Y. Fujiki, Raman-spectrum of anatase, TiO_2. J. Raman Spectrosc. **7**, 321–324 (1978). https://doi.org/10.1002/jrs.1250070606
36. M. Giarola, A. Sanson, F. Monti, G. Mariotto, M. Bettinelli, A. Speghini, G. Salviulo, Vibrational dynamics of anatase TiO_2: Polarized Raman spectroscopy and ab initio calculations. Phys. Rev. B **81**, 174305 (2010). https://doi.org/10.1103/PhysRevB.81.174305
37. U. Pal, A. Sandoval, S.I. Uribe Madrid, G. Corro, V. Sharma, P. Mohanty, Mixed titanium, silicon, and aluminum oxide nanostructures as novel adsorbent for removal of rhodamine 6G and methylene blue as cationic dyes from aqueous solution. Chemosphere **163**, 142–152 (2016). https://doi.org/10.1016/j.chemosphere.2016.08.020
38. D. Bersani, P.P. Lottici, X. Ding, Phonon confinement effects in the Raman scattering by TiO_2 nanocrystals Appl. Phys. Lett. **72**, 73 (1998). https://doi.org/10.1063/1.120648
39. S.P.S. Porto, P.A. Fleury, T.C. Dame, Raman spectra of TiO_2, MgF_2, ZnF_2, FeF_2, and MnF_2. Physical Rev **154**, 522 (1967). https://doi.org/10.1103/PhysRev.154.522
40. D.O. Scanlon, C.W. Dunnill, J. Buckeridge, S.A. Shevlin, A.J. Logsdail, S.M. Woodley, C. Richard, A. Catlow, M.J. Powell, R.G. Palgrave, I.P. Parkin, G.W. Watson, T.W. Keal, P. Sherwood, A. Walsh, A.A. Sokol, Band alignment of rutile and anatase TiO_2. Nat. Mater. **12**, 798–801 (2013). https://doi.org/10.1038/nmat3697
41. A. Vahl, S. Veziroglu, B. Henkel, T. Strunskus, O. Polonskyi, O.C. Aktas, F. Faupel, Pathways to tailor photocatalytic performance of TiO2 thin films deposited by reactive magnetron sputtering. Materials **12**, 2840 (2019). https://doi.org/10.3390/ma12172840